SELF CONSISTENT MODEL FOR THE EVOLUTION OF ECCENTRIC MASSIVE BLACK HOLE BINARIES IN STELLAR ENVIRONMENTS: IMPLICATIONS FOR GRAVITATIONAL WAVE OBSERVATIONS

Alberto Sesana
Max Planck Institute for Gravitationalphysik (Albert Einstein Institute), Am Mühlenberg, 14476, Golm, Germany
Received 2010 April 26; accepted 2010 June 3; published 2010 July 23

ABSTRACT

We construct evolutionary tracks for massive black hole binaries (MBHBs) embedded in a surrounding distribution of stars. The dynamics of the binary is evolved by taking into account the erosion of the central stellar cusp bound to the massive black holes, the scattering of unbound stars feeding the binary loss cone, and the emission of gravitational waves (GWs). Stellar dynamics is treated in a hybrid fashion by coupling the results of numerical three-body scattering experiments of bound and unbound stars to an analytical framework for the evolution of the stellar density distribution and for the efficiency of the binary loss-cone refilling. Our main focus is on the behavior of the binary eccentricity, in the attempt of addressing its importance in the merger process and its possible impact for GW detection with the planned *Laser Interferometer Space Antenna* (*LISA*), and ongoing and forthcoming pulsar timing array (PTA) campaigns. We produce a family of evolutionary tracks extensively sampling the relevant parameters of the system which are the binary mass, mass ratio and initial eccentricity, the slope of the stellar density distribution, its normalization and the efficiency of loss-cone refilling. We find that, in general, stellar dynamics causes a dramatic increase of the MBHB eccentricity, especially for initially already mildly eccentric and/or unequal mass binaries. This affects the overall system dynamics; high eccentricities enhance the efficiency of GW emission, accelerating the final coalescence process. When applied to standard MBHB population models, our results predict eccentricities in the ranges 10^{-3}–0.2 and 0.03–0.3 for sources detectable by *LISA* and PTA, respectively. Such figures may have a significant impact on the signal modeling, on source detection, and on the development of parameter estimation algorithms.

Key words: black hole physics – galaxies: evolution – galaxies: kinematics and dynamics – gravitational waves – methods: numerical

Online-only material: color figures

1. INTRODUCTION

It is now widely recognized that massive black holes (MBHs) are fundamental building blocks in the process of galaxy formation and evolution. MBHs are a ubiquitous components of nearby galaxy nuclei (see, e.g., Magorrian et al. 1998), and their masses tightly correlate with the properties of the host (Haring & Rix 2004, and references therein). In popular ΛCDM cosmologies, structure formation proceeds in a hierarchical fashion (White & Rees 1978), through a sequence of merging events. If MBHs are common in galaxy centers at all epochs, as implied by the notion that galaxies harbor active nuclei for a short period of their lifetime (Haehnelt & Rees 1993), then a large number of massive black hole binaries (MBHBs) are expected to form during cosmic history. The evolution of such binaries was first sketched by Begelman et al. (1980), but after thirty years, several details of the involved dynamical processes are still unclear.

In stellar environments, the MBHB evolution proceeds via super-elastic scattering of surrounding stars intersecting the binary orbit (slingshot mechanism, Mikkola & Valtonen 1992), and the fate of the system depends on the supply of stars available for such interaction. On the other hand, if the system is gas rich, torques exerted by a massive circumbinary disk have been proven efficient in shrinking the binary down to ∼0.1 pc (Escala et al. 2005; Dotti et al. 2007), which is the current resolution limit of dedicated smoothed particle hydrodynamical simulations. However, whether viscous angular momentum extraction is efficient all the way down to coalescence is questionable (Lodato et al. 2009).

In general, the vast majority of studies (mostly numerical) devoted to the subject have focused on the shrinking of the binary semimajor axis, because the relatively small number of particles involved ($N < 10^6$) makes the eccentricity behavior fairly noisy. However, eccentricity may play an important role in the final coalescence, because at a given semimajor axis, the coalescence timescale associated with gravitational wave (GW) emission is much shorter for very eccentric binaries (Peters & Mathews 1963). Moreover, having a trustworthy model for the eccentricity evolution of the system may be of crucial importance for the practical detection of MBHBs in the forthcoming GW windows.

MBHBs are in fact expected to be the loudest sources of gravitational radiation in the nHz–mHz frequency range (Haehnelt 1994; Jaffe & Backer 2003; Wyithe & Loeb 2003; Enoki et al. 2004; Sesana et al. 2004, 2005; Jenet et al. 2005; Rhook & Wyithe 2005; Sesana et al. 2008, 2009). The space-borne observatory *Laser Interferometer Space Antenna* (*LISA*, Danzmann et al. 1998) has been planned to cover the range of frequencies from 10^{-4} Hz to 0.1 Hz. Moving to the nanohertz frequency range, the Parkes Pulsar Timing Array (Manchester 2008), the European Pulsar Timing Array (Janssen et al. 2008), and the North American Nanohertz Observatory for Gravitational Waves (Jenet et al. 2009) are already collecting data and improving their sensitivity in the of 10^{-8}–10^{-6} Hz window, and in the next decade the planned Square Kilometer Array (Lazio 2009) will provide a major leap in sensitivity.

Besides the technical progresses in the instrumentation, the source signal modeling and the development of appropriate data analysis techniques for recovering the sources from the

data stream are crucial for the success of the GW astronomy challenge. So far, most of the attention has been focused on circular MBHBs. This seems to be justified, because GW emission is very efficient in dampening the binary eccentricity, and since GW detectors (*LISA* in particular) are sensitive to the very end of the MBHB inspiral, sources are expected to be circular when they enter the observable band. Consequently, most of the source modeling and the signal searches and analyses, e.g., the source injection in the *LISA* mock data challenge (Babak et al. 2010), or the investigation carried out by the *LISA* parameter estimation task force (Arun et al. 2009), relied on this assumption.

However, both stellar and gas based shrinking mechanisms have proven to be efficient in increasing the binary eccentricity (Quinlan 1996; Armitage & Natarajan 2005; Sesana et al. 2006, 2008; Baumgardt et al. 2006; Matsubayashi et al. 2007; Berentzen et al. 2009; Cuadra et al. 2009; Amaro-Seoane et al. 2009, 2010), calling into question whether the assumption of circular orbits is justified for such GW sources. In this paper, we construct a self-consistent simple model for tracking the evolution of the MBHB eccentricity (and semimajor axis) in *stellar* environments. We model the stellar distribution surrounding the bound binary as an isothermal sphere ($\rho \propto r^{-2}$) matching a cusp with a power-law density profile $\rho \propto r^{-\gamma}$ inside the binary influence radius. The MBHB is evolved taking into account the scattering of bound stars leading to the erosion of the cusp (Sesana et al. 2008), the subsequent scattering of unbound stars intersecting the binary semimajor axis (Quinlan 1996; Sesana et al. 2006), and the efficient GW emission stage (Peters & Mathews 1963) leading to final coalescence of the system. The main goal of the paper is to build sensible evolutionary tracks for the MBHB as a function of the binary mass, mass ratio, initial eccentricity at pairing and cusp slope, and to show that viable MBHB evolution scenarios predict a significant eccentricity in the frequency band relevant to GW observations with *LISA* and PTAs.

The paper is organized as follows. In Section 2, we extensively describe our model, defining the relevant physical mechanisms and writing down the evolution equations for the system. In Section 3, we provide further insights about the physics of the model, linking our treatment to the loss-cone refilling theory. We present our evolutionary tracks in detail in Section 4, discussing the dependencies on the relevant model parameters, and we draw predictions for *LISA* and PTA observations in Section 5. Our main findings are summarized in Section 6.

2. INGREDIENTS OF THE MODEL

2.1. Initial Setup

We consider an MBHB with mass $M = M_1 + M_2$ ($M_1 > M_2$) described by its semimajor axis a and eccentricity e. The system is embedded in a purely stellar background with a density profile described by a double power law, as follows:

$$\rho(r) = \rho_{\text{inf}} \left(\frac{r}{r_{\text{inf}}}\right)^{-\gamma} \quad r < r_{\text{inf}}$$
$$\rho(r) = \frac{\sigma^2}{2\pi G r^2} \quad r > r_{\text{inf}}. \quad (1)$$

Here, r_{inf} is the influence radius of the binary, identifying the region where the gravitational potential is dominated by the two MBHs, and formally defined as the radius containing a stellar mass equal to M, and ρ_{inf} is the stellar density at r_{inf}. The density distribution is normalized to an isothermal sphere for $r > r_{\text{inf}}$,

such a condition sets

$$\rho_{\text{inf}} = \frac{\sigma^2}{2\pi G r_{\text{inf}}^2} \quad (2)$$

and

$$r_{\text{inf}} = (3 - \gamma) \frac{GM}{\sigma^2} \approx 0.8\,\text{pc}\,(3 - \gamma) M_6^{1/2}, \quad (3)$$

where M_6 is the total mass of the binary in units of $10^6\,M_\odot$, and we made use of the well established M–σ relation in the form (Tremaine et al. 2002)

$$M_6 = 0.84 \sigma_{70}^4 \quad (4)$$

(σ_{70} is the velocity dispersion in units of 70 km s^{-1}) to get rid of σ in the last approximation. We identify the region $r < r_{\text{inf}}$ as the inner cusp, and we use $\gamma = 1$, 1.5, and 2 corresponding to nuclei characterized by cores/weak cusps, mild cusps, and steep cusps, respectively.

N-body simulations of unequal mass binaries in the mass ratio range 0.01–10^{-3} (Baumgardt et al. 2006; Matsubayashi et al. 2007) have shown that dynamical friction is efficient in driving the secondary MBH much deeper than r_{inf} in the potential well of the primary-cusp system. The two MBH pairs together form an MBHB and continue to harden down to a separation at which the enclosed mass in the binary is of the order of M_2, without significantly affecting the stellar density profile. This is an indication that the hardening is still driven by the dynamical friction exerted by the overall distribution of stars, rather than by close individual encounters with stars intersecting the binary orbit. In our model, we assume that M_2 is driven by dynamical friction down to a separation a_0 where the enclosed stellar mass in the binary is twice the mass of the secondary MBH,

$$a_0 = (3 - \gamma) \frac{GM}{\sigma^2} \left(\frac{q}{1 + q}\right)^{1/(3-\gamma)} = r_{\text{inf}} \left(\frac{q}{1 + q}\right)^{1/(3-\gamma)}, \quad (5)$$

($q = M_2/M_1$ is the mass ration of the binary system) without affecting the stellar distribution in the cusp significantly. At that point, three-body interactions take over, and the binary evolution is dictated by individual encounters with stars intersecting its orbit.

2.2. Physical Mechanisms in Operation

On its way to final coalescence starting from a_0, the binary is subject to three main dynamical mechanisms driving its evolution, namely: (1) the erosion of the cusp bound to the primary MBH, (2) the scattering of unbound stars supplied into the binary loss cone by relaxation processes once the stellar distribution is significantly modified by the MBHB, and (3) the emission of GWs. The detailed description of each mechanism has been presented elsewhere, and the reader will be referred throughout this section to the appropriate references for further insights. The focus of the present work is to add them together coherently, to produce sensible, although admittedly very simplistic, evolutionary tracks for MBHBs hardening in stellar environments.

2.2.1. Bound Cusp Erosion

The hardening of an unequal mass MBHB, with an initial semimajor axis a_0 and eccentricity e_0, in a bound cusp was extensively studied by Sesana et al. (2008), hereinafter SHM08.

Using their formalism, two differential equations determine the rate of change of the orbital separation and eccentricity:

$$\frac{da}{dt}\Big|_b = -\frac{2a^2}{GM_1M_2}\int_0^\infty \Delta\mathcal{E}\frac{d^2N_{\rm ej}}{da_*dt}da_*,\qquad(6)$$

$$\frac{de}{dt}\Big|_b = \int_0^\infty \Delta e\frac{d^2N_{\rm ej}}{da_*dt}da_*.\qquad(7)$$

Here, a_* is the semimajor axis of a star bound to M_1 and $d^2N_{\rm ej}/da_*dt$ is the number of stars subject to slingshot ejection in the semimajor axis and time intervals $[a_*, a_* + da_*]$, $[t, t + dt]$. The terms Δe, $\Delta\mathcal{E}$ are measured from scattering experiments. The ejection rate $d^2N_{\rm ej}/da_*dt$ is instead computed by coupling the numerical results of the experiments to an analytic framework for the binary evolution, which is embedded in a cusp of the form described by Equation (1), as detailed in SHM08. The major finding of SHM08 is that the binary hardens by a factor of $\sim$10 by extracting the binding energy of the stars in the cusp. During this process, e usually increases by a large factor, depending on the binary mass ratio and on the cusp slope. Results are tabulated in Table 1 of SHM08.

2.2.2. Slingshot of Unbound Stars

The theory of MBHB hardening in a distribution of unbound field stars characterized by a density ρ and a velocity dispersion σ was singled out by Quinlan (1996) and extensively revisited by Sesana et al. (2006), hereinafter SHM06. The binary evolution can be expressed as a function of the dimensionless hardening rate H and eccentricity growth rate K as

$$\frac{da}{dt}\Big|_u = -\frac{a^2G\rho}{\sigma}H,\qquad(8)$$

$$\frac{de}{dt}\Big|_u = \frac{aG\rho}{\sigma}HK.\qquad(9)$$

The quantities H and K are related to the average energy and angular momentum exchange between the stars and the binary in a single encounter and are computed via extensive three-body scattering experiments, as described, e.g., in SHM06. In general, hardening by scattering of unbound stars becomes effective when the binary reaches the so-called hardening radius, defined as (Quinlan 1996)

$$a_h \approx \frac{GM_2}{4\sigma^2}.\qquad(10)$$

This is the separation at which the specific binding energy of the binary is of the order of the specific kinetic energy of the field stars. For $a > a_h$, stars are basically too fast to effectively exchange energy and angular momentum with the binary (soft binary regime); when $a < a_h$, the binary tends to capture stars in short living weakly bound orbits, kicking them to infinity with $v > \sigma$ (hard binary regime). The transition soft/hard binary is rather smooth and happens at about a_h. Once the binary is hard, its hardening proceeds at about constant rate, as shown by the H tracks plotted in Figure 3 of SHM06. Perfectly circular binaries tend to stay circular (because of the conservation of the Jacobian integral of motion in the three-body problem), while even slightly eccentric binaries tend to increase their eccentricity, as shown by the K rates plotted in Figure 4 of SHM06.

2.2.3. Gravitational Wave Emission

For our purposes, the effect of GW emission can be modeled in the quadrupole approximation. Under this assumption, the evolution equations for the system are given by Peters & Mathews (1963):

$$\frac{da}{dt}\Big|_{\rm GW} = -\frac{64}{5}\frac{G^3}{c^5}\frac{M_1M_2M}{a^3(1-e^2)^{7/2}}\left(1+\frac{73}{24}e^2+\frac{37}{96}e^4\right)$$

$$= -\frac{64}{5}\frac{G^3}{c^5}\frac{M_1M_2M}{a^3}F(e)\qquad(11)$$

$$\frac{de}{dt}\Big|_{\rm GW} = -\frac{304}{15}\frac{G^3}{c^5}\frac{M_1M_2M}{a^4(1-e^2)^{5/2}}e\left(1+\frac{121}{304}e^2\right).\qquad(12)$$

The function $F(e)$ is defined by the last equality in Equation (11). The shrinking rate is a strong factor of a, meaning that GW-driven hardening is effective only at small separations. The eccentricity evolution rate is also a strong function of a and e itself, and it is always negative. GW emission, therefore, is very effective in circularizing MBHBs, which, in turn, is the reason why little attention has been paid so far to eccentric systems in the context of GW detection.

2.3. General Equations for the Binary Evolution

Having identified the relevant mechanisms at play, we can put the pieces together by writing the evolution of the binary as

$$\frac{da}{dt} = \sum_i \frac{da}{dt}\Big|_i\qquad(13)$$

$$\frac{de}{dt} = \sum_i \frac{de}{dt}\Big|_i,\qquad(14)$$

where $i = b, u, {\rm GW}$ labels the three mechanisms considered. Here, we handle MBHBs in stellar environments, and the relevant scale of the stellar distribution is defined by the sphere of influence $r_{\rm inf}$ of the MBHBs. It is then natural to consider as relevant parameters the stellar density and velocity dispersion at the influence radius, $\rho_{\rm inf}$ and $\sigma_{\rm inf} = \sigma$ (for an isothermal sphere, the velocity dispersion is independent on radius). It is then instructive to recast the MBHB dynamics in the dimensionless H and K formalism proposed by Quinlan, to compare the dimensionless rates given by each mechanism.

The global evolution of the system can be then written as a generalization of Equations (8) and (9) in the form

$$\frac{da}{dt} = -\frac{a^2G\rho_{\rm inf}}{\sigma}\sum_i H_i\qquad(15)$$

$$\frac{de}{dt} = \frac{aG\rho_{\rm inf}}{\sigma}\sum_i H_iK_i,\qquad(16)$$

where H_i is trivially defined as

$$H_i = \frac{\sigma}{a^2G\rho_{\rm inf}}\frac{da}{dt}\Big|_i\qquad(17)$$

and

$$K_i = a\frac{de}{dt}\Big|_i\left(\sum_j \frac{da}{dt}\Big|_j\right)^{-1}.\qquad(18)$$

We integrate the coupled differential Equations (15) and (16) starting from a_0. As described in Section 2.1(Equation (5)), the value of a_0 is set by the total mass of the binary M, the mass ratio $q = M_2/M_1$, the cusp slope γ, and the stellar velocity dispersion σ. In our default models, we force σ to obey the M–σ relation given by Equation (4). In this manner, there is a one-to-one correspondence between the mass of the binary and σ, i.e., equally massive binaries are embedded in identical isothermal spheres. Having set the normalization of the stellar distribution and the initial separation a_0, the evolution of the binary depends on the four parameters M_1, q, e_0, and γ. We extensively sample this parameter space as following:

1. $\log(M_1/M_\odot) = 2, 3, 4, 5, 6, 7, 8, 9, 10, 11$
2. $q = 1, 1/3, 1/9, ..., 1/729$
3. $e_0 = 0.01, 0.1, 0.3, 0.6, 0.9$
4. $\gamma = 1, 1.5, 2$

for a grand total of $10 \times 7 \times 5 \times 3 = 1050$ simulations. Even though the binary evolution under the effect of stellar encounters is basically scale free, the simulation of systems with different absolute masses was necessary to match together the scattering-driven phase to the GW-driven phase, which instead is highly mass dependent. The assumption of different eccentricities at the moment of pairing takes the environmental effects affecting the dynamical friction stage into account. In general, during the merging process, galaxies capture each other on a very eccentric orbit, which is reflected in the initial trajectories of the two MBHs (still at kpc separations at this stage). Dynamical friction against massive, rotationally supported, circumbinary disks has been proven to circularize the orbit (Dotti et al. 2006). However, this is not in general true in gas poor environments, where the process is driven by interaction with the stellar distribution (Colpi et al. 1999), and the eccentricity of the MBHB at the moment of pairing may retain memory of its initial value, or may, in general, be different from zero.

We also consider four alternative models to address the impact of the assumed M–σ relation and the choice of normalizing the efficiency of unbound scatterings to $\rho_{\rm inf}$. Let us denote with $\hat{\sigma}$ the value of the velocity dispersion predicted by the M–σ relation for a given M. We consider models with velocity dispersions equal to $0.7\hat{\sigma}$ and $1.3\hat{\sigma}$, which is approximately the range of variance of σ for a given MBH mass measured in the M–σ relation (Haring & Rix 2004). We also run models with two different normalizations for the unbound scattering process: a fast model normalized to $10\rho_{\rm inf}$ and a slow model normalized to $0.1\rho_{\rm inf}$. The motivation for this set of runs will be clarified in Section 3.2.

To practically evolve the binary, we make use of the results of the scattering experiments with unbound and bound stars performed in SHM06 and SHM08. In those papers, the quantities Δe, $\Delta \mathcal{E}$, $d^2 N_{\rm ej}/da_* dt$ (for the bound scatterings), H and K (for the unbound scatterings) were recorded on a grid of a and e, covering the relevant dynamical range. The evolution of the coupled differential Equations (15) and (16) is performed by interpolation over the grid as the binary evolves. In SHM06, unbound scatterings were carried out for all the considered mass ratios down to $q = 1/243$. To complete the sample, we carried out additional experiments for the case $q = 1/729$. SHM08, instead, focused on unequal MBHBs, with $q \lesssim 0.1$. To complete the mass ratio sample, we ran experiments for the cases $q = 1, 1/3$. We then have all the bound and unbound scattering experiments' results spanning the q and e_0 range of interest.

2.4. Limitations and Caveats

Our evolutionary tracks are computed in a self-consistent way, summing together the effects of different mechanisms. However, we should be aware of the several limitations and simplifications we have adopted. One major caveat is the extension of the bound scattering experiments to mass ratios of $q > 1/9$. It is in fact unlikely that, in such cases, M_2 would reach a_0 without affecting the stellar cusp at all. Cusp disruption would start earlier (especially in the equal mass case), and the cusp erosion phase described here may not be a trustworthy description of reality. However, we find that the impact of the bound cusp erosion on the binary evolution is smaller for larger mass ratios. This is because for $q \to 1$, $a_0 \sim r_{\rm inf}$ (see Figure 1), and the impact of the binding energy extraction in the total energy budget of the system becomes less significant. The eccentricity evolution in the cusp erosion phase is only mild when $q = 1, 1/3$, implying that our approximate treatment would not significantly affect the overall results. Another caveat to bear in mind is that the three-body scattering is a scale-free problem as long as $m_* \ll M_2$. Even though we compute "a posteriori" evolutionary tracks for systems with $M_1 = 100\,M_\odot$ and $q = 1/729$, we consider our results meaningful only when $M_2 > 100\,M_\odot$. This is also reasonable, since we are interested in the evolution of MBHBs. Moreover, if M_2 is small ($<10^4\,M_\odot$), the amount of stars interacting with the binary is also quite small, i.e., the granularity of the problem increases. Our smooth evolutionary tracks should then be interpreted more as "trends" or "mean evolutions" rather than paths followed by each individual binary. We have also not included the possibility of stellar tidal disruption, which has been shown to be an efficient process in the cusp erosion phase, especially in the mass ratio range $0.01 < q < 0.1$ (Chen et al. 2009). In general, the inclusion of tidal disruptions mildly enhances the increase of eccentricity (Chen et al. 2010), because disrupted stars preferentially have $a_* < a$, i.e., they would drive the binary toward circularization if ejected (see SHM08 for a detailed discussion of this effect). Lastly, there is a somewhat net distinction between bound and unbound scatterings in our formalism, which is certainly oversimplistic, since in reality relaxation processes will mix up the different stellar populations. The appearance of distinctive features in the transition between the bound and the unbound regime can be therefore considered somewhat artificial; the reality would probably be more gentle. We do not believe that this has a major impact on our main results.

3. PHYSICS OF THE BINARY EVOLUTION

The relative contributions of the three mechanisms considered in the previous section are set by the typical lengthscales below which they become effective. As stated before, cusp erosion becomes effective at a_0. At this point, H_b and K_b start to dominate the MBHB evolution.

On the other hand, scattering of unbound stars becomes fully effective at the hardening radius a_h defined by Equation (19):

$$a_h \approx \frac{1}{4(3-\gamma)}\left(\frac{q}{1+q}\right)^{(2-\gamma)/(3-\gamma)} a_0$$

$$\approx 0.2\,{\rm pc}\,M_6^{1/2}\left(\frac{q}{1+q}\right). \tag{19}$$

We see that $a_h = (1/4)a_0$ independently of the mass ratio for $\gamma = 2$, and in general, with decreasing γ, the ratio a_h/a_0 becomes smaller and q dependent. As the binary shrinks,
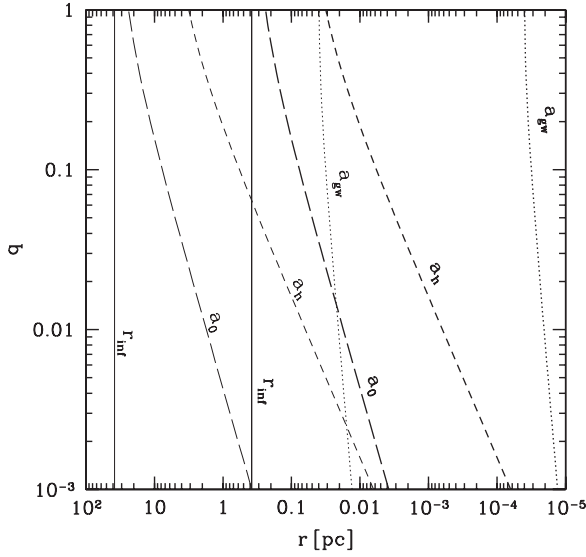
Figure 1. Relevant lengthscales in the binary hardening problem as a function of the binary mass ratio for two different absolute values of the binary mass $M = 10^5 \, M_\odot$ (thick lines) and $M = 10^9 \, M_\odot$ (thin lines). For each set of curves, from left to right, we plot $r_{\rm inf}$, a_0, a_h, and $a_{\rm GW}$ (for a circular binary, i.e., assuming $F(e) = 1$, see Equation (11)), as labeled in the figure. The cusp slope is fixed to $\gamma = 1.5$.

the central cusp is depleted and the scattering of unbound stars refilling the binary loss cone (i.e., the family of stellar orbits intersecting the binary semimajor axis, see the next section) becomes dominant. In this second stage, occurring at approximately $0.1a_0$ the binary evolution is determined by H_u and K_u.

Gravitational radiation will eventually take over at $a_{\rm GW}$, driving the binary to the final coalescence. $a_{\rm GW}$ can be derived by imposing $da/dt|_u = da/dt|_{\rm GW}$; rearranging and dividing by a_h we find

$$a_{\rm GW} = 4 \left[\frac{128\pi(3-\gamma)F(e)}{5H} \right]^{1/5} \frac{\sigma}{c} q^{-4/5} (1+q)^{3/5} a_h$$
$$\approx 0.00027 \, {\rm pc} \, (3-\gamma)^{1/5} F(e)^{1/5} M_6^{3/4} \frac{q^{1/5}}{(1+q)^{2/5}}, \quad (20)$$

where $F(e)$ is defined by Equation (11), and we again used the M–σ relation to write the last approximation. Figure 1 highlights the behavior of the lengthscales of the system ($r_{\rm inf}$, a_0, a_h, $a_{\rm GW}$) as a function of q for two selected values of M and $\gamma = 1.5$. It is easy to see that, in general, $a_{\rm GW} \ll a_h$. For example, assuming circular binaries with $q = 1$, $H = 15$, and $\sigma = 100$ km s^{-1} (or $M = 4 \times 10^6 \, M_\odot$, according to the M–σ) gives $a_{\rm GW}/a_h \approx 2 \times 10^{-3}$. $a_{\rm GW}$ can approach a_h if the mass ratio is extreme ($q \sim 10^{-3}$) and the velocity dispersion is very large (e.g., if the binary is massive; $\sigma > 300$ km s^{-1} or $M > 10^9 \, M_\odot$), as shown by the set of thin lines in Figure 1. In general, Figure 1 clearly shows that there are three well-defined zones where one single shrinking mechanism is dominant among the others and we have

$$a_{\rm GW} < a_h < a_0 < r_{\rm inf}. \quad (21)$$

3.1. H and K Formalism in the Loss-cone Framework

It is instructive at this point to frame the hardening rate given by Equation (8) in the context of loss-cone refilling theory (Frank & Rees 1976; Lightman & Shapiro 1977; Cohn

& Kulsrud 1978). After the binary has depleted all the stars intersecting its orbit (formally defining what is called the "binary loss cone" of the stellar distribution function, see Milosavljevic & Merritt 2003 for a comprehensive review), its further hardening depends on the rate Γ at which such orbits (i.e., the loss cone) are refilled. Loss-cone refilling can proceed by diffusion of stars either in energy (ϵ_*) or in angular momentum (j_*). In general, stellar encounters are much more efficient in changing the star angular momentum, and diffusion in the j_* space is the relevant process. The loss-cone refilling depends on the average Δj_* experienced by a star on an almost radial orbit during one orbital period. If this change is larger than the size of the binary loss cone in the angular momentum space, $j_{\rm lc} \sim \sqrt{2GMa}$, then stars are easily scattered back and forth into the loss cone and the loss cone is filled. In this regime, the supply rate of stars from a given distance to the binary r is given by Lightman & Shapiro (1977) and Perets & Alexander (2008):

$$\frac{d\Gamma_f}{d\log r} \approx \frac{a}{r} \frac{N_*(<r)}{P(r)}. \quad (22)$$

Here, $P(r)$ is the typical period of a star on an almost radial orbit coming from a distance r and $N_*(<r)$ is the number of stars enclosed in a sphere of radius r around the MBHB. Let us focus on stars coming from $r > r_{\rm inf}$. Assuming that an isothermal sphere $N_*(<r) = (M/m_*)(r/r_{\rm inf})$ and that the typical period of a star on a radial orbit is $P(r) \sim r/\sigma$, integrating Equation (22) from $r_{\rm inf}$ to ∞ and using Equation (2), we get

$$\Gamma_f \approx 2\pi \frac{M}{m_*} \frac{G\rho_{\rm inf}a}{\sigma}. \quad (23)$$

Let us contrast this result with Equation (8). In the Quinlan formulation, the binary is embedded in a homogeneous stellar field with density ρ. The hardening rate H is then derived writing the interaction rate as a flux of stars through the binary cross section, namely

$$\Gamma_Q = \frac{\rho}{m_*} \Sigma v, \quad (24)$$

where ρ/m_* is the number density of field stars, v their velocity at infinity (i.e., far from the binary), and Σ the binary cross section. If b is the star impact parameter at infinity and if we assume the encounter to be relevant only for $b < b_{\rm max}$, then $\Sigma = \pi b_{\rm max}^2$. Relating b to the maximum approach x to the binary via gravitational focusing ($b^2 = 2GMx/v^2$) and replacing $x_{\rm max} = a$ (stars have to cross the binary semimajor axis to exchange energy and angular momentum efficiently), we get

$$\Gamma_Q = 2\pi \frac{M}{m_*} \frac{G\rho a}{v}. \quad (25)$$

By comparing Equations (23) and (25), if we identify the intruder velocity at infinity v with the dispersion velocity in the isothermal sphere σ, we see that our H_u and K_u prescriptions for the scattering of unbound stars correspond to considering the loss cone always full at $r_{\rm inf}$.

3.2. Loss-cone Refilling

By normalizing H_u and K_u to σ and $\rho_{\rm inf}$, our model implicitly assumes that the loss cone is always full at $r > r_{\rm inf}$ (i.e., in the so-called *pinhole* regime) and empty for $r < r_{\rm inf}$ (i.e., in the so-called *diffusive* regime, Cohn & Kulsrud 1978). The status of the loss cone then enters as a parameter in our formulation, set by
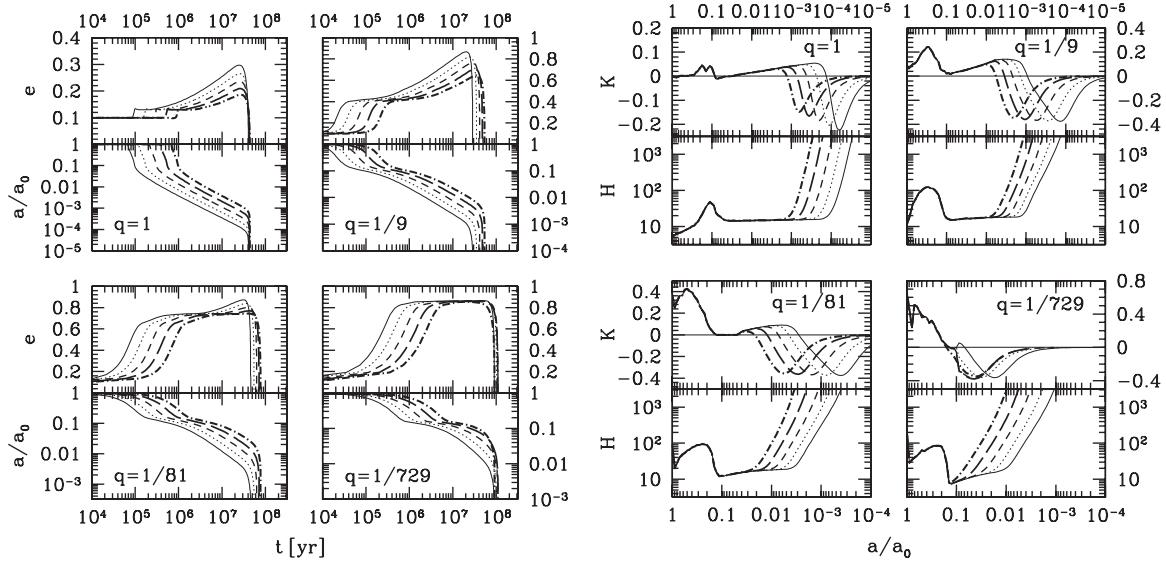
Figure 2. MBHB evolutionary tracks produced by our model by assuming $\gamma = 1.5$ and $e_0 = 0.1$. Left plot: in each of the four pairs of panels, we plot the eccentricity (top) and semimajor axis (bottom) evolution as a function of time. Different panels refer to different values of q, as marked by the inset labels. Different linestyles correspond to different binary masses: $M = 10^5\,M_\odot$ (solid), $10^6\,M_\odot$ (dotted), $10^7\,M_\odot$ (short-dashed), $10^8\,M_\odot$ (long-dashed), and $10^9\,M_\odot$ (dotted-dashed). Right plot: corresponding binary eccentricity growth rate K (top panels in each of the four sectors) and hardening rate H (bottom panels in each of the four sectors), as a factor of the binary separation normalized to a_0. Linestyles as in the left plot.

our choice of normalizing the system to ρ_{inf}. The issue of what is the physical mechanism that keeps the loss cone full at $r > r_{\text{inf}}$ is not addressed in this paper. We will only briefly discuss here the plausibility of such a scenario. After the loss cone is depleted, in the absence of any other physical mechanism, two-body relaxation (Binney & Tremaine 2008) sets the timescale for loss-cone refilling. This is usually longer than the Hubble times in real galaxies (Merritt & Szell 2006), and under this assumption, the loss cone is, in general, in the diffusive regime way beyond r_{inf}. However, in more realistic situations, a myriad of other physical factors play a substantial role, shortening the loss-cone refilling timescale. It has been shown that axisymmetry and in particular triaxiality (Yu 2002; Merritt & Poon 2004; Berczik et al. 2006) are very effective in repopulating the loss cone, driving stars on chaotic and centrophilic orbits toward the black hole. Moreover, the matter distribution in stellar bulges is far from being smooth. Inhomogeneous concentrations of matter, such as massive star clusters or giant molecular clouds (the so-called massive perturbers), have been proven efficient in perturbing stellar orbits, significantly shortening the loss-cone refilling timescale (Perets & Alexander 2008). We should note that these mechanisms are likely to operate efficiently for $r > r_{\text{inf}}$. Inside the MBH influence radius, indeed, the presence of a central massive object dominating the gravitational potential tends to force the stellar system toward a more spherical symmetry (and the triaxial structure may be erased in the central region, see, e.g., Merritt & Quinlan 1998). For the same reason, massive perturbers tend to be stripped by the MBH tidal field and would hardly survive in this region. Also, the two-body relaxation timescale increases for decreasing r if the potential is dominated by a central object, because the velocity dispersion of the system, which in this region is the Keplerian velocity around the MBH, scales as $r^{-1/2}$, and the relaxation timescale has a strong dependence on the velocity dispersion (Binney & Tremaine 2008). Moreover, inside r_{inf}, the ejection of stars bound in the cusp depletes those orbits with energy $\epsilon_* < GM/(2r_{\text{inf}})$, and since ϵ_* diffusion is much less efficient than j_* diffusion the contribution to the loss-cone

refilling coming from $r < r_{\text{inf}}$ should be, in general, negligible. It is then reasonable to assume a full loss cone for $r > r_{\text{inf}}$, and otherwise empty. We shall test the implication of such a hypothesis by varying the normalization used in Equations (15) and (16). We therefore test models normalized to $10\rho_{\text{inf}}$ and $0.1\rho_{\text{inf}}$, which correspond to consider the loss cone full only for $r > 10^{1/2}r_{\text{inf}}$ and down to $r = 10^{-(3-\gamma)/2}r_{\text{inf}}$ (where γ is the slope of the inner cusp as defined by Equation (1)), respectively. The consideration of smaller values of the relevant density assumed for the diffusion process ($0.1\rho_{\text{inf}}$) also serves as a test for the robustness of our results against different outer density profiles. Although our refilling rate is derived for an isothermal distribution, which reasonably fits the measured density profiles of several nearby galaxies and of the Milky Way (Lauer et al. 1995; Dehnen & Binney 1998), many other galaxies show shallower outer density profiles (Ferrarese et al. 1994; Gebhardt et al. 1996; Rest et al. 2001) and the bulk of stars participating to the refilling mechanism may come from slightly larger radii, where the density is lower. We will show (Section 5.2 and Figure 7) that this has a minor impact on our results, changing the eccentricity of the system in the observable GW bands by a factor $\lesssim 2$.

4. EVOLUTIONARY TRACKS FOR MBHBs

In this section, we present the MBHB evolutionary tracks produced by our hybrid model. As discussed in the previous section, the binary goes through three subsequent phases, which are in general distinct. In the discussion, we will simply identify them as the bound phase (erosion of the bound cusp), unbound phase (scattering of unbound stars refilling the loss cone), and GW phase (where GW emission becomes more efficient than the unbound scattering). Each phase is characterized by its proper H_i and K_i. In the following compilation of plots, we will present the evolution of the global rates $H = \sum_i H_i$ and $K = \sum_i K_i$; it will be clear by looking at the figures which particular mechanism dominates in each region of the binary evolution. Each of the Figures 2, 3, and 4 shows the quantities $e(t)$, $a/a_0(t)$, $K(a/a_0)$,
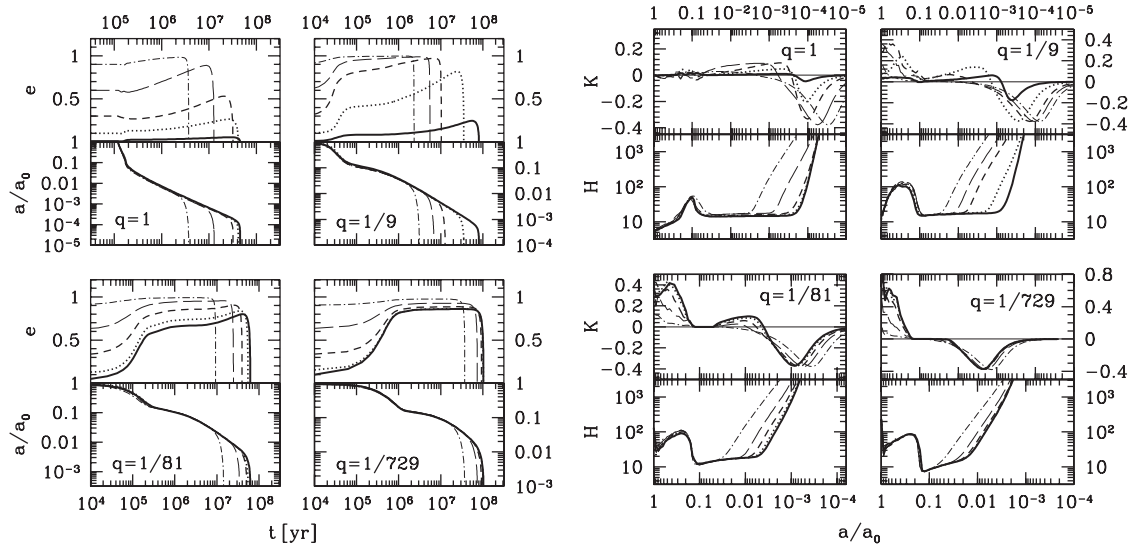
Figure 3. Same as Figure 2, but now assuming $M = 10^6\ M_\odot$ and varying the initial eccentricity e_0. In each individual panel, different linestyles are for $e_0 = 0.01$ (solid), 0.1 (dotted), 0.3 (short-dashed), 0.6 (long-dashed), and 0.9 (dotted-dashed). The inner cusp slope is fixed to $\gamma = 1.5$.
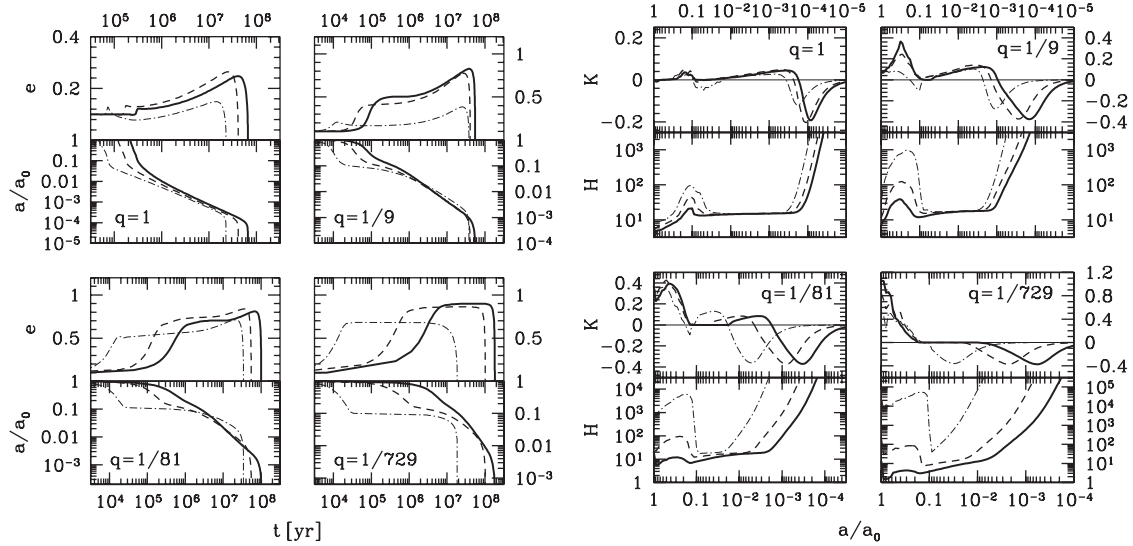
Figure 4. Same as Figure 2, but now assuming $M = 10^6\ M_\odot$, $e_0 = 0.1$ and varying the cusp slope. Different linestyles are for $\gamma = 1$ (solid), 1.5 (dashed), and 2 (dotted-dashed).

and $H(a/a_0)$ for different q, as labeled in each panel. In the discussion, we will simply refer to the panels as e, a, H, and K panels.

4.1. Dependence on the Model Parameters

The evolution of the system depends on the chosen values for the parameters M_1, q, e_0, and γ. Such dependencies are extensively illustrated in Figures 2, 3, and 4. Let us consider each parameter separately, by starting with those defining the masses of the system: M_1 and q.

The evolution of the MBHB as a function of M_1 and for different q is plotted in Figure 2, assuming $\gamma = 1.5$ and $e_i = 0.1$. Since our treatment of stellar scattering is scale free, the value of M_1 affects the system evolution *only*, by setting the relative gap between a_h and a_{GW}, which has a mild dependence on M_1. By substituting the M–σ relation in Equation (20), we have in fact $a_h/a_{\mathrm{GW}} \propto M^{-1/4}$, i.e., the gap is larger for lighter systems. This means that, in general, lighter binaries become more eccentric, because, after the bound scattering phase (which is basically

scale free by construction) they evolve under the effect of unbound scattering for a larger portion of their dynamical range, as it becomes clear by looking at the K panels of Figure 2. For equal mass binaries with $e_0 = 0.1$, the eccentricity grows only to 0.15 for $M_1 = 10^9\ M_\odot$ and up to 0.3 for $M_1 = 10^5\ M_\odot$. The mass dependence of the eccentricity growth is also evident for binaries with $q = 1/9$, while it tends to disappear for lower mass ratios where the eccentricity evolution is dominated by the bound phase. The q dependence of the eccentricity evolution is emphasized by the four different quadrants of Figures 2, 3, and 4. Let us consider again Figure 2. The main result here is that the eccentricity growth in the bound phase, at least when e_0 is small, is in general much larger for lower values of q, as explained in detail in Section 4.1 of SHM08. This is nicely shown by the K panels: as q decreases from 1 to 1/729, the peak in the K rate increases from $\sim$0.05 to $\sim$0.6. The value of q also sets the relative weight of the bound and of the unbound phases in the hardening process. Although a_0/a_h is only mildly dependent on q (depending on the cusp slope γ, see Equation (19)), a_h/a_{GW}

is a strong function of q (see Equation (20)) and it can be even less than one for high M_1 and small q (as shown in Figure 1). Therefore, as q decreases, the eccentricity growth is dominated by the bound phase. For $e_0 = 0.1$, the maximum eccentricity reached by the binary at the end of the stellar driven phase increases from ~ 0.2 for $q = 1$ to ~ 0.9 for $q = 1/729$. The trends with M_1 and q presented in Figure 2 are preserved when changing γ and e_0.

The dependence of the MBHB evolution on e_0 is studied in Figure 3, where we fixed $M_1 = 10^6 \, M_\odot$ and $\gamma = 1.5$. The binary eccentricity, in general, tends to increase in the scattering phase regardless of the value of e_0. When $e_0 = 0.01$, binaries with $q > 0.1$ experience only a mild increase in their eccentricity, up to a value ~ 0.2, while binaries with smaller q can reach $e > 0.8$. Binaries with $e_0 > 0.3$ tend to reach eccentricities larger than 0.9 regardless of q, M_1, and γ. The evolution of H is basically unaffected by the eccentricity of the system in the bound and unbound phases (in general the average energy subtracted to the binary by the star is not affected by the binary eccentricity, see e.g., SHM06); while K is interestingly larger for higher e_0 when q is large, and vice versa, it decreases with increasing e_0 for small q.

The impact of the assumed slope γ of the density profile is highlighted in Figure 4 for binaries with $M_1 = 10^6 \, M_\odot$ and $e_0 = 0.1$. In general, MBHBs in steeper cusps evolve faster, but to a lower maximum eccentricity, during the scattering phase. As explained in SHM08 this is because, in the scattering process, stars with $a_* > a$ tend to increase e while stars with $a_* < a$ tend to decrease it, and the relative weight of the former is larger in shallower cusps. Moreover, by increasing γ, the dynamical range covered by the scattering process is much shorter (especially for low q), because the a_0–$a_{\rm GW}$ gap is smaller, and there is less room for significant eccentricity growth. The K rates are mildly affected by γ, with a higher value of γ resulting in smaller K, as explained before. Also note that the absolute value of H in the bound phase increases a lot with γ. This is because the value of a_0 is much smaller for high γ, and the shrinkage in the bound phase is accordingly much faster. In general, for any value of γ, the eccentricity reached at the end of the star scattering phase is >0.7 for $q < 0.1$, while, again, equal mass binaries experience a less pronounced increase in the eccentricity.

Figures 2, 3, and 4 allow also a detailed study of the evolutionary timescale as a function of the system parameters. Since the bound phase is usually much faster than the unbound one, the evolution timescale of the system is set by $a/\dot{a} = \sigma/(G\rho Ha) \propto 1/a$. The coalescence timescale is then set by the bound-GW transition occurring at $a_{\rm GW}$. By substituting $a_{\rm GW}$ given by Equation (20) in the timescale definition above, we get for the coalescence timescale

$$\tau_c \propto F(e)^{-1/5}(3-\gamma)^{9/5}q^{-1/5}(1+q)^{2/5}. \qquad (26)$$

Firstly, we note that τ_c is independent of the absolute value of the MBHB mass, in agreement with Figure 2. This is a consequence of normalizing the stellar distribution outside $r_{\rm inf}$ to an isothermal sphere obeying the M–σ relation. τ_c also has a very mild dependence on q, increasing by a factor of ~ 3 when the mass ratio drops from $q = 1$ to $q = 1/729$, as shown by the correspondent panels in Figure 2. High values of the maximum eccentricity accelerate the coalescence by a factor $F(e)^{1/5}$, which is ~ 5 for $e = 0.9$; this effect is clear in the (a) and (e) panels of Figure 3. The impact of γ is also quite mild, in spite of the 9/5 exponent, and it modifies τ_c by a factor of

~ 3–4 (see (a) and (e) panels in Figure 4). In general, we find 10^7 yr $< \tau_c <$ few $\times 10^8$ yr.

4.2. Comparison with Numerical Works

The evolution of MBHBs in stellar environments has been tackled by several authors by means of full N-body simulations (Milosavljevic & Merritt 2001; Hemsendorf et al. 2002; Aarseth 2003; Makino & Funato 2004; Baumgardt et al. 2006; Matsubayashi et al. 2007; Merritt et al. 2007; Berentzen et al. 2009; Amaro-Seoane et al. 2009, 2010). However, the limited number of particles ($N < 10^6$) in such simulations results in very noisy behavior for the binary eccentricity, and it is difficult to draw conclusions about the general trends behind the numerical noise. We can compare our results with N-body simulations carried out in two regimes: $q = 1$ (equal mass inspirals) and $q = 1/1000$ (intermediate MBH–MBH inspiral). Milosavljevic & Merritt (2001) carried out numerical integration of equal MBHBs embedded in two merging isothermal cusps ($\gamma = 2$). Starting with circular orbits, they find a mild eccentricity increase to a value of $\lesssim 0.2$ during the stellar-driven hardening phase, consistent with our findings. Merritt et al. (2007) considered equal MBHBs embedded in Dehnen density profiles (Dehnen 1993) with $\gamma = 1.2$ with different initial eccentricities. Again, they find that circular binaries tend to stay circular, while eccentric binaries tend to increase their eccentricities in reasonable agreement with the prediction of scattering experiments, and, consequently, with the tracks we presented in Figure 3 for the $q = 1$ case. Simulations carried out by Aarseth (2003) and Hemsendorf et al. (2002) produce MBHBs with $e_0 \approx 0.8$ at the moment of pairing, with e subsequently increasing up to $\gtrsim 0.95$, again consistent with our findings. Berentzen et al. (2009) studied the evolution of equal MBHBs in rotating systems described by a King stellar distribution. They also find quite eccentric binaries at the moment of pairing ($e > 0.4$), and the subsequent evolution leads to eccentricities larger than 0.95 at which point GW emission takes over, again consistent with our findings. Amaro-Seoane et al. (2009) focused on intermediate MBHBs ($M \sim 10^3 \, M_\odot$) in massive star clusters. They employ a machinery similar to ours, coupling full N-body simulations to three-body scattering experiments. Their binaries have significant eccentricity (~ 0.5–0.6) at the moment of pairing, and the predicted range in the *LISA* band is $0.1 < e < 0.3$, in good agreement with the results shown by the eccentricity maps in Figure 5 that we will describe in the next section. Similar conclusions are reported by Amaro-Seoane et al. (2010). On the small q side, simulations were performed by Baumgardt et al. (2006) and Matsubayashi et al. (2007), assuming a stellar density profile $\gamma = 1.75$. When properly rescaled, the eccentricity increase found in both papers agrees surprisingly well with our predictions based on the hybrid cusp erosion model. Unfortunately, we did not find any mention in the N-body literature about the eccentricity evolution for intermediate values of q ($0.01 < q < 0.1$), and it would be useful to compare our results with N-body simulations in this intermediate range. We find, however, the overall good agreement, at least in the trends, shown at the two extremes of the mass ratio range comforting.

5. ECCENTRICITY IN THE *LISA* AND PTA WINDOWS

One of the main goals of the present study is to draw sensible predictions for the eccentricity of MBHBs emitting GWs in the *LISA* and in the PTA frequency ranges. So far, most of the work related to source modeling, signal analysis and parameter
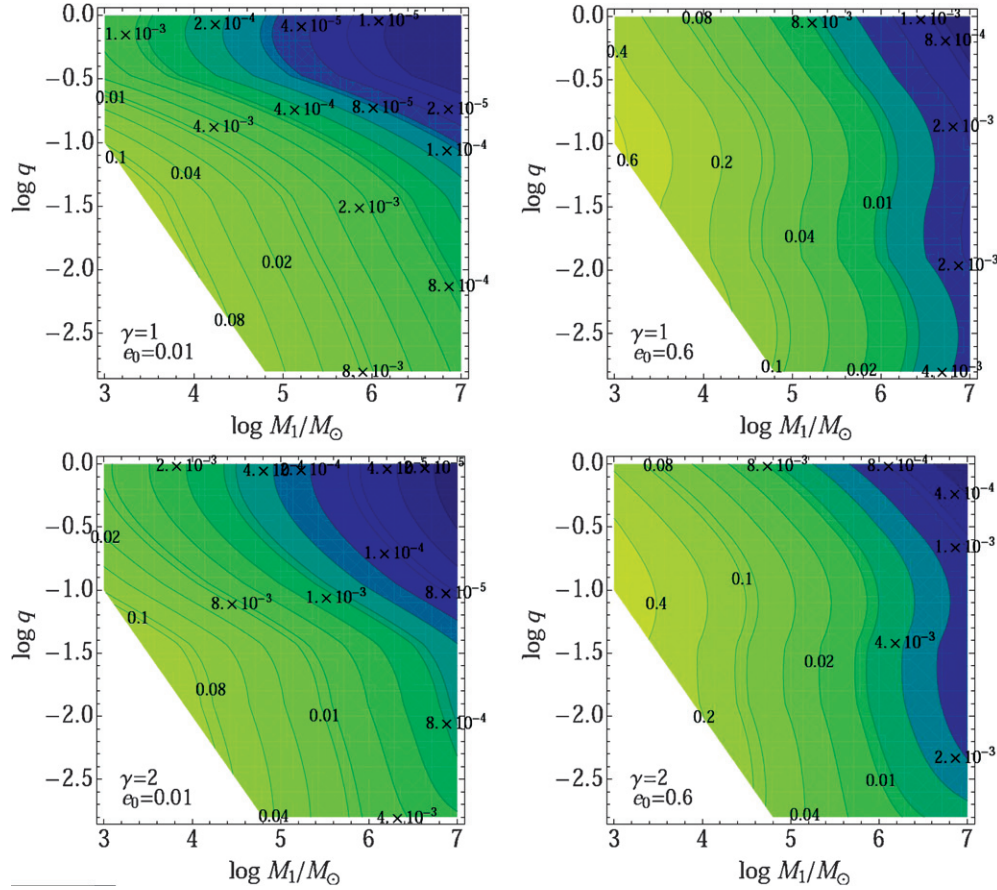
Figure 5. Contour plots of e computed at $f_{\mathrm{LISA}} = 5 \times 10^{-5}$ Hz, in the (M_1, q) plane for selected model parameters, as labeled in each panel. Note that we excluded the bottom-left region, corresponding to systems for which $M_2 < 100\, M_\odot$.
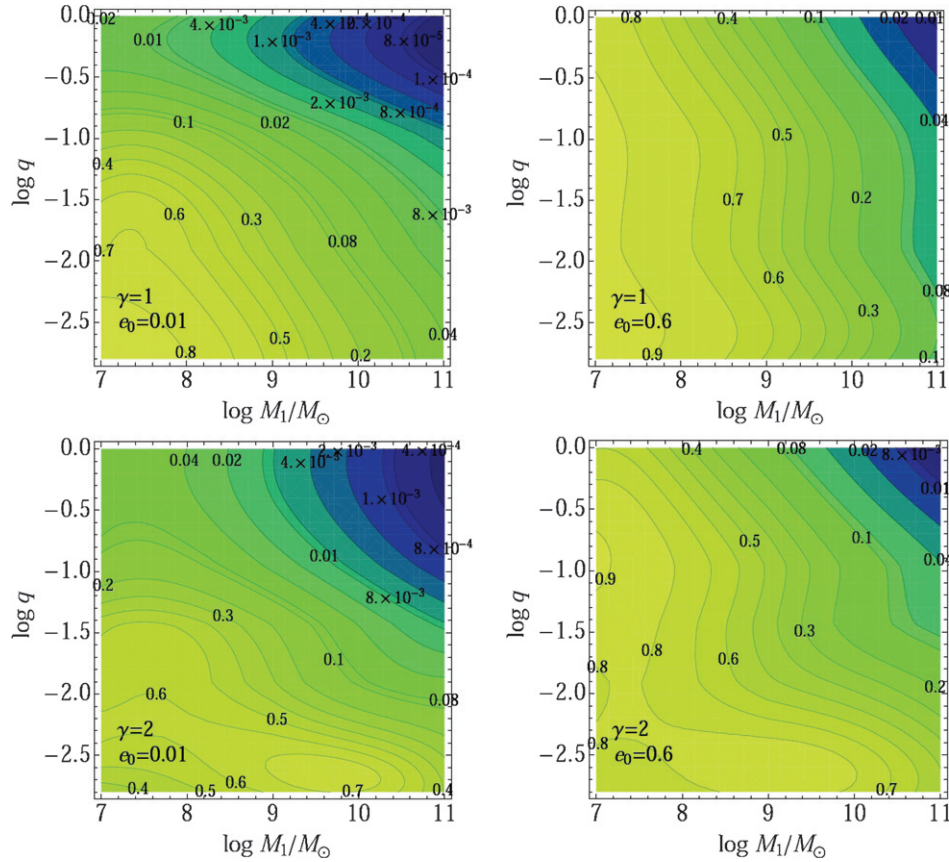(A color version of this figure is available in the online journal.)

estimation relied on the assumption of circular orbits. This seems reasonable because GW emission is very efficient in dampening the binary eccentricity, and since GW detectors (*LISA* in particular) are sensitive to the very end of the MBHB inspiral, sources are assumed to be circular when they enter the observable band. However, the level of residual eccentricity critically depends on how large e is at the transition between the stellar hardening and the GW phases. In the scenario proposed here, such values can easily be larger than 0.9, implying non-negligible residual eccentricities in the frequency bands to be probed by future GW detectors.

5.1. Eccentricity Maps

To convert our evolutionary track into predictions for GW observations, we proceed as follows. For each MBHB (uniquely defined by M_1, q, γ, and e_0), we convert the $a/a_0(t)$ tracks into $a(t)$ tracks, and then we compute $f_k(t)$, the orbital frequency of the binary, simply by assuming Kepler's law. Having $e(t)$ and $f_k(t)$, we then construct the $e(f_k)$ evolution from the moment of pairing to the final coalescence. We then select two frequencies appropriate for *LISA* and PTA campaigns, f_{LISA} and f_{PTA}, respectively, and evaluate $e|_{f_{\mathrm{LISA}}}$ and $e|_{f_{\mathrm{PTA}}}$. Remember that for circular binaries, gravitational radiation is emitted at $f_{\mathrm{GW}} = 2f_k$. We pick $f_{LISA} = 5 \times 10^{-5}$ Hz (corresponding to $f_{\mathrm{GW}} = 10^{-4}$ Hz, which is approximately the lower bound of the *LISA* band); on the other hand, we use $f_{\mathrm{PTA}} = 5 \times 10^{-9}$ Hz (corresponding to $f_{\mathrm{GW}} = 10^{-8}$ Hz, which is approximately the frequency at which a 5-to-10 yr PTA campaign will be most

sensitive to). The results are shown in Figures 5 and 6 as contour plots $e|_{f_{LISA}}(M_1, q)$ and $e|_{f_{\mathrm{PTA}}}(M_1, q)$, for selected values of γ and e_0, as labeled in the figures. Let us start discussing the *LISA* case. First, we limited M_1 to an upper value of $10^7\, M_\odot$, since the inspiral of binaries with higher masses will fall outside the *LISA* band.[1] We also excluded from our contour plots systems with $M_2 < 100\, M_\odot$, for the reasons discussed in Section 2.4. The general trend is that lighter unequal mass binaries tend to have larger e when they enter the relevant frequency range. The mass trend is easily explained by the fact that our treatment is largely mass invariant, but the absolute frequency of the system is not. Same stages of the MBHB evolution correspond to progressively lower frequencies as M_1 increases, and since we are in the GW-dominated phase (and thus $de/df < 0$), more massive systems have lower eccentricities at a given frequency. Binaries with smaller q are in general more eccentric because the eccentricity growth they experience in the stellar scattering phase is larger. If binaries are approximately circular at the moment of pairing ($e_0 = 0.01$), then the maximum eccentricity in the *LISA* band is ~ 0.2 when $M_1 \sim 10^4\, M_\odot$ and $q \lesssim 0.1$, and the general trend is largely independent on γ. This is the result of two competitive effects: milder cusps lead to larger values of e, but in this case GW takes over earlier (because the timescale of the three-body

---

[1] The higher frequency signal coming from the coalescence and ringdown as well as higher harmonic corrections to the late inspiral phase (Porter & Cornish 2008) are likely to push the detectable mass limit close to $10^8\, M_\odot$; however, the imprint of any residual eccentricity would be very small and hard to observe for such extreme masses.

Figure 6. Same as Figure 5, but now for $f_{PTA} = 5 \times 10^{-9}$ Hz. Note the different scale in the x-axis, dictated by the fact that PTAs are sensitive to more massive systems emitting at lower frequencies.

(A color version of this figure is available in the online journal.)

scattering evolution is set by the density at r_{inf} which is lower for milder central cusps, being r_{inf} itself larger), and it has more time to circularize the orbit before the binary get to f_{LISA}. If binaries are significantly eccentric at the moment of pairing ($e_0 = 0.6$ as a study case), then the q dependence in the contour plots almost disappear, because the eccentricity growth in the scattering phase is very efficient irrespective of q when e_0 is large. In this case, light MBHBs ($M_1 < 10^4$) may reach f_{LISA} with eccentricities up to ~0.5.

The situation is even more "dramatic" for PTA observations. PTAs are sensitive to much larger masses ($M_1 > 10^7 M_\odot$) emitting at much lower frequencies ($f \approx 10^{-8}$ Hz). Systems are, in general, caught far from coalescence (the typical time to coalescence is ~10^4 yr, Sesana & Vecchio 2010) and they did not have much time to circularize under the effect of GW emission. Because of this, even if binaries were circular at the moment of pairing, eccentricities can be as high as 0.7 in the PTA band, with the same trend observed for the *LISA* case (i.e., lighter binaries with smaller q are more eccentric). If $e_0 = 0.6$, then all the systems with $M_1 < 10^9 M_\odot$ are expected to have $e > 0.5$. Again, the results are only mildly dependent on γ. Note that frequencies are computed in the reference frame of the source, the actual observed frequency has then to be appropriately redshifted by a factor $(1 + z)$ according to the redshift of the emitting system. This means that for high redshift sources, an *observed* frequency of 10^{-4} Hz corresponds to a higher *intrinsic* frequency. High redshift sources may then have milder eccentricities in the observable band, which may be relevant for *LISA* sources (whereas typical PTA sources are at $z < 1$).

5.2. The Impact of the Chosen Normalization

We want to check at this point how the M–σ normalization and the tuning of the loss-cone refilling efficiency to r_{inf} impact on our results. Selected cases of alternative models are presented in Figure 7. The left-hand plot is representative of *LISA* sources. We see that changing σ merely shifts the timescale of the binary evolution. For larger σ, the system is more compact, the timescale for three-body scattering is shorter, GW emission takes over later, and consequently the residual e at f_{LISA} is larger. However, as shown by the $e(f_k)$ tracks, this is at most a factor-of-2 effect. Changing the normalization ρ in the loss-cone refilling process has instead a major impact on the evolutionary timescale and on the eccentricity evolution of the system, but still the residual eccentricity at f_{LISA} is basically unaffected when $e_0 = 0.01$, and it changes by at most a factor of 3 in the $e_0 = 0.6$ case. In the right-hand plot, we consider instead the typical PTA source. All the considerations made for the *LISA* case still hold, and in the relevant frequency range 3×10^{-9} Hz $< f < 3 \times 10^{-8}$ Hz, the expected e changes by at most a factor of 2. We therefore consider our results quite robust irrespective of the assumed normalizations.

5.3. Eccentricity Distributions for Selected MBHB Population Models

As a final step, we quantify the eccentricity distribution of GW sources in the relevant frequency range resulting by applying our eccentricity evolution scheme to standard MBHB population models.
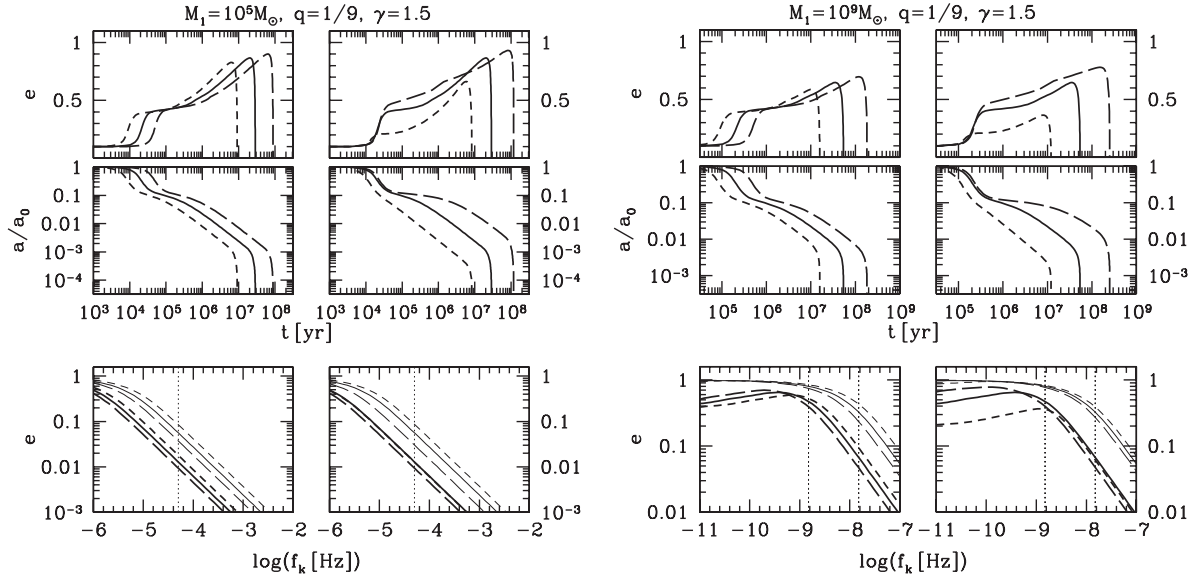
Figure 7. Impact on the M–σ assumption and on the ρ normalization on the evolution of the binary. Left plot: representative *LISA* source, with system parameter highlighted at the top. Right plot: typical PTA sources, with system parameters highlighted at the top. In each plot, in the left panels we considered three different normalizations of the stellar velocity dispersion: $\sigma = \hat{\sigma}$ (i.e., the value predicted by the M–σ relation, solid lines), $1.3\hat{\sigma}$ (short-dashed lines), and $0.7\hat{\sigma}$ (long-dashed lines); in the right panel we stick the efficiency of loss-cone refilling to $\rho_{\rm inf}$ (solid lines), $10\rho_{\rm inf}$ (short-dashed lines), and $0.1\rho_{\rm inf}$ (long-dashed lines). Top and middle panels represent the evolution of e and a against t, respectively; bottom panels represent $e(f_k)$. In these latter panels, $f_{\rm LISA}$ and the relevant frequency PTA range $3 \times 10^{-9}\,{\rm Hz} < f < 3 \times 10^{-8}\,{\rm Hz}$ are highlighted.

For the *LISA* case, we use two of the models utilized by the *LISA* parameter estimation task force (Arun et al. 2009): in the first case seeds are light ($M \gtrsim 100\,M_\odot$, VHM model; Volonteri et al. 2003), being the remnant of the first POPIII star explosions (Madau & Rees 2001); in the second case already quite heavy ($M \gtrsim 10^4\,M_\odot$) seed BHs form by direct collapse of massive protogalactic discs (BVR model; Begelman et al. 2006). We ran 50 Monte Carlo realizations of each model, producing 50 catalogs of coalescing binaries over a period of three years. We then estimate the signal-to-noise ratio (S/N) of each binary in the *LISA* detector by assuming circular inspiral and computing the waveform to the second post-Newtonian order. We then consider only those events resulting in an S/N > 8 in the detector, and we compute the expected eccentricity distribution at $f_{\rm LISA}$. Results are shown in Figure 8. In the upper and in the middle panels, we plot the contour plots of the differential distribution of GW sources as a function of M_1 and q, d^2N/dM_1dq, averaged over the 50 Monte Carlo realizations, superposed to the contour plots for $e|_{f_{\rm LISA}}(M_1, q)$. The two observed MBHB populations are extremely different: in the VHM model, the bulk of sources have $M \sim 10^4\,M_\odot$ with $q \sim 0.1$; while in the BVR model, most of the sources have $M > 10^4\,M_\odot$ and $q \approx 1$. The resulting eccentricity distributions are plotted in the lower panel, where we plot the probability density function $p(e)$ against e for the observed population. When $e_0 = 0.01$ (binaries approximately circular), eccentricity is expected to be $<10^{-2}$ in the BVR model, with a peak at about 2×10^{-3}, but a broad eccentricity spectrum covering the range 10^{-3}–0.2 is expected in the VHM case. In this latter scenario, in fact, sources are on average less massive and with low q, a condition that maximizes the eccentricity increase during the stellar scattering phase. If e_0 is already large (0.6 in our study case), then the observed eccentricity at $f_{\rm LISA}$ is peaked at $\sim$0.1 for the BVR case and at $\sim$0.4 in the VHM case.

In exploring the consequences for PTA observations, we adopt the standard Tu-SA population model employed by Sesana

et al. (2009), where merging galaxies are populated by MBHs according to the $M - M_{\rm bulge}$ in the form given by Tundo et al. (2007) and accretion is triggered onto the more MBH *before* the final coalescence. The reader is referred to Sesana et al. (2009) for details. We ran 50 Monte Carlo realizations of the model (assuming binaries in circular orbit) and we pick only the individually resolvable sources generating a timing residual larger than 1 ns. Again, the obtained differential distribution of the individually resolvable sources, d^2N/dM_1dq, averaged over the 50 Monte Carlo realizations, is superposed to the contour plots for $e|_{\rm PTA}(M_1, q)$ in Figure 9. The source distribution is strongly peaked around $M_1 = 10^9\,M_\odot$ and $q = 0.1$, with a long tail extending to $q = 10^{-3}$. If binaries are approximately circular at the moment of pairing ($e_0 = 0.01$), then the expected $p(e)$ is basically flat in the range [0.03, 0.3], while for $e_0 = 0.6$, $p(e)$ has a sharp peak in the range [0.5, 0.7], highlighting the possible significant impact of eccentricity for PTA observations.

6. DISCUSSION AND CONCLUSIONS

We studied the semimajor axis and eccentricity evolution of MBHBs in stellar environments by coupling the results of numerical three-body scattering experiments to an analytical framework describing the evolution of the stellar distribution and the supply of stars to the binary loss cone. Our treatment takes into account the scattering of bound stars determining the erosion of the stellar cusp bound to the binary, and the subsequent scattering of unbound stars fed to the binary loss cone by relaxation processes. We do not address the nature of the relaxation processes leading to loss-cone replenishment, but we treat the loss-cone refilling efficiency as a parameter of the model. Eventually, GW emission takes over, leading to the final coalescence of the system.

Our main finding is that three-body scattering induces a significant increase in the MBHB eccentricity, which is not efficiently washed out by GW-induced circularization before
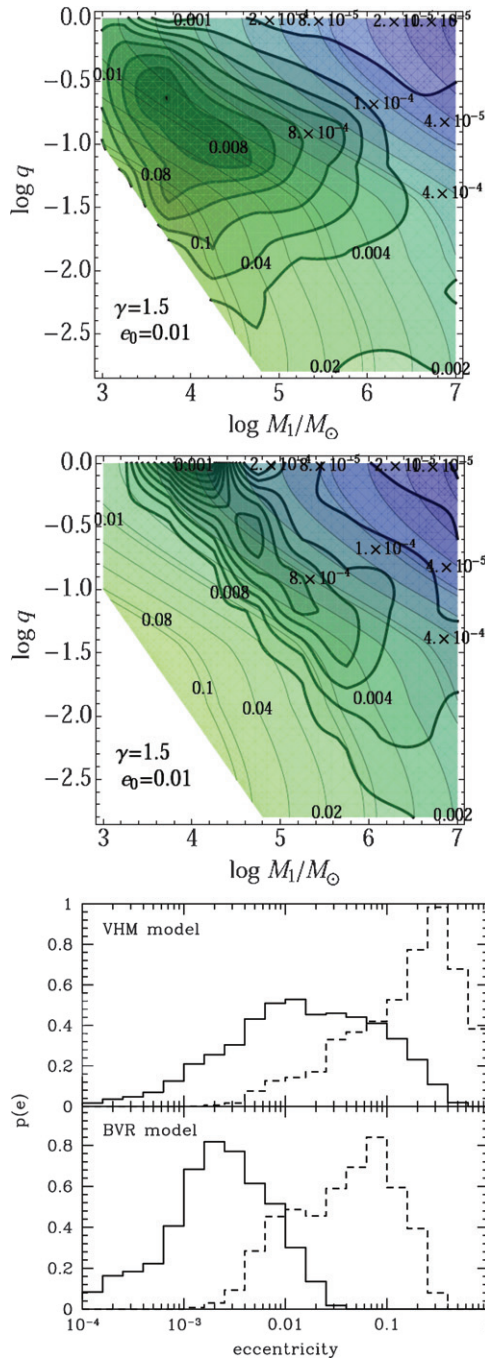
Figure 8. Evaluation of the eccentricity distribution of MBHBs observed by *LISA*. Top and middle panels: contour plots of the differential distribution of observable sources $d^2N/dM_1 dq$ (gray scale, contour normalization unnecessary for illustrative purposes), superimposed to the contour plots of $e|_{f_{LISA}}$ (color scale; $\gamma = 1.5$, $e_0 = 0.01$) in the (M_1, q) plane. Inset labels refer to the e contours. Top panel is for the VHM model, middle panel is for the BVR model. Bottom panel: probability density function $p(e)$ corresponding to the contour plot convolution; solid histograms are for $e_0 = 0.01$ and dashed histograms are for $e_0 = 0.6$.

(A color version of this figure is available in the online journal.)

the system enter the *LISA* or the PTA bands. The eccentricity growth is in general larger for binaries with smaller mass ratios, and at the stellar scattering-GW transition can easily be higher than 0.9. Equal mass binaries in general experience a milder eccentricity growth when the initial eccentricity is close to zero. The eccentricity growth is more prominent for systems characterized by smaller masses. Binaries with significant initial
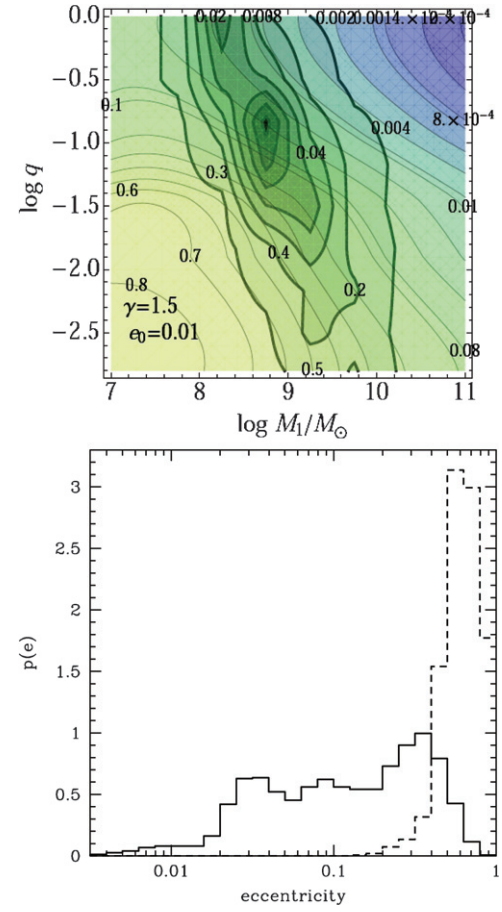
Figure 9. Same as Figure 8, but for PTA observations. In the top panel, the differential distribution of observable sources $d^2N/dM_1 dq$ is now superposed to $e|_{f_{PTA}}$, again assuming $\gamma = 1.5$ and $e_0 = 0.01$. The resulting $p(e)$ is plotted in the bottom panel assuming $e_0 = 0.01$ (solid histogram) and $e_0 = 0.6$ (dashed histogram).

(A color version of this figure is available in the online journal.)

eccentricity $e_0 > 0.3$ end up in very eccentric orbits ($e > 0.9$) regardless of the other system parameters. The impact of the cusp slope can be significant, with shallower cusps leading to higher maximal values of e, as explained in SHM08. In general, the eccentricity growth is dominated by the bound scattering phase for binaries with $q < 0.1$ and by the unbound scattering phase for binaries with larger mass ratios. When compared to the sparse results of full N-body simulations found in literature, the results of our models are in reasonable agreement with those of numerical studies.

The implications for GW observations are relevant. When binaries are circular at the moment of pairing, their eccentricity when they enter the *LISA* band is in the range 10^{-5}–0.2, and it is larger for low-mass unequal binaries. If binaries are already eccentric at the moment of pairing, these figures shift to the range 10^{-3}–0.5, with lower mass binaries leading to higher eccentricities and only a mild dependence on the mass ratio. We emphasize once again that in our treatment, the total mass of the system sets the typical scale of the problem; because of this, the residual eccentricity in the *LISA* band is *larger for lighter binaries*. This is important because *LISA* will be mostly sensitive to low-mass MBHBs in the range 10^4–$10^5 \, M_\odot$. In the PTA windows, the implications are even stronger. Initially, circular systems end up with eccentricities in the range 10^{-3}–0.8 at a frequency of 10^{-8} Hz (relevant to PTA observations), and

for significant initial eccentricity, binaries with $M_1 < 10^{-9} M_\odot$ always have $e > 0.5$ in the PTA band. The trend with the mass and the mass ratio are the same as for their *LISA* counterparts. All the results are basically independent of the cusp slope γ and are only mildly dependent on the normalization of the stellar density distribution and on the efficiency of the loss-cone refilling.

Once applied to standard MBHB population models, these results predict eccentricities in the range 10^{-3}–0.2 (depending on the adopted seed formation model) for observable *LISA* sources, and a broad flat e distribution in the interval 0.03–0.3 for sources individually resolvable by PTAs. High initial values of e naturally lead to more eccentric systems.

Our results are of particular interest for the GW community, showing that a proper treatment of the eccentricity might be crucial in the challenge of GW detection. Mock data challenge initiatives like the *LISA* mock data challenge have so far implemented circular MBHBs only, and consequently, the ability of data analysis and parameter estimation algorithms has been proven only in this situation. The typical eccentricity values found in the *LISA* band (<0.2 for systems in circular orbit at the moment of pairing) allow for a perturbative approach to the problem of constructing a trustworthy post-Newtonian waveform, such as the one recently employed by Yunes et al. (2009). In light of the results presented here, further work in this direction would be extremely valuable. The addition of a non-zero eccentricity would affect the waveform by adding significant amplitude modulation and phase precession, which in turn would affect our detection and parameter estimation ability (work in this direction is ongoing; Porter & Sesana 2010). Also in the PTA source modeling field, the assumption of circular orbits has been widely used so far, with the notable exception of Enoki & Nagashima (2007). Further work on eccentric source modeling is needed, in order to address properly how an eccentric population of MBHB would affect the overall level of the background, the statistics of individually resolvable sources, the detailed shape of the residuals, and our ability to extract signals and estimate source parameters.

We finally stress that our model is oversimplified, relying only on stellar dynamics without taking into account the possible impact of the presence of large amounts of gas surrounding the binary. Gas dynamics may be particularly relevant to *LISA* sources, which are expected to be found in mergers of small galaxies at high redshift (Sesana et al. 2007), where the mass content of galaxies is likely to be dominated by gas (see, e.g., Cole et al. 2000). In this view, our model should provide a more trustworthy description of PTA sources which consist instead of massive binaries at low redshift (Sesana et al. 2009), likely hosted by gas-poorer galaxies. Nonetheless, we should bear in mind that recent studies also found significant eccentricity increase in MBHBs driven by circumbinary disks (Armitage & Natarajan 2005; Cuadra et al. 2009). Moreover, gas dynamics may not be efficient enough to drive the final coalescence of MBHB systems (Lodato et al. 2009), and also for low-mass sources at high redshift, stellar dynamics may provide a viable alternative path through the final coalescence. We hope that our exploratory study will stimulate further research on the subject, which is of critical importance for a comprehensive modeling of MBHB evolution and for their future observation in the upcoming gravitational radiation windows.

REFERENCES

Aarseth, S. J. 2003, Ap&SS, 285, 367
Amaro-Seoane, P., Eichhorn, C., Porter, E. K., & Spurzem, R. 2010, MNRAS, 401, 2268
Amaro-Seoane, P., Miller, M. C., & Freitag, M. 2009, ApJ, 692, 50
Armitage, P. J., & Natarajan, P. 2005, ApJ, 634, 921
Arun, K. G., et al. 2009, Class. Quantum Gravity, 26, 4027
Babak, S., et al. 2010, Class. Quantum Gravity, 27, 4009
Baumgardt, H., Gualandris, A., & Portegies Zwart, S. 2006, MNRAS, 372, 174
Begelman, M. C., Blandford, R. D., & Rees, M. J. 1980, Nature, 287, 307
Begelman, M. C., Volonteri, M., & Rees, M. J. 2006, MNRAS, 370, 289
Berczik, P., Merritt, D., Spurzem, R., & Bischof, H. P. 2006, ApJ, 642, 21
Berentzen, I., Preto, M., Berczik, P., Merritt, D., & Spurzem, R. 2009, ApJ, 695, 455
Binney, J., & Tremaine, S. 2008, Galactic Dynamics (2nd ed., Princeton, NJ: Princeton Univ. Press)
Chen, X., Madau, P., Sesana, A., & Liu, F. K. 2009, ApJ, 697, 149
Chen, X., Sesana, A., Madau, P., & Liu, F. K. 2010, ApJ, submitted
Cohn, H., & Kulsrud, R. M. 1978, ApJ, 226, 1087
Cole, S., Lacey, C. G., Baugh, C. M., & Frenk, C. S. 2000, MNRAS, 319, 168
Colpi, M., Mayer, L., & Governato, F. 1999, ApJ, 525, 720
Cuadra, J., Armitage, P. J., Alexander, R. D., & Begelman, M. C. 2009, MNRAS, 393, 1423
Danzmann, K., et al. 1998, LISA-Laser Interferometer Space Antenna, Pre-Phase A Report (2nd ed.; Garching: Max-Planck-Institute fur Quantenaptik)
Dehnen, W. 1993, MNRAS, 265, 250
Dehnen, W., & Binney, J. 1998, MNRAS, 298, 387
Dotti, M., Colpi, M., & Haardt, F. 2006, MNRAS, 367, 103
Dotti, M., Colpi, M., Haardt, F., & Mayer, L. 2007, MNRAS, 379, 956
Enoki, M., Inoue, K. T., Nagashima, M., & Sugiyama, N. 2004, ApJ, 615, 19
Enoki, M., & Nagashima, M. 2007, Prog. Theor. Phys., 117, 241
Escala, A., Larson, R. B., Coppi, P. S., & Mardones, D. 2005, ApJ, 630, 152
Ferrarese, L., van den Bosch, F. C., Ford, H. C., Jaffe, W., & O'Connell, R. W. 1994, AJ, 108, 2403
Frank, J., & Rees, M. J. 1976, MNRAS, 176, 633
Gebhardt, K., et al. 1996, AJ, 112, 105
Haehnelt, M. G. 1994, MNRAS, 269, 199
Haehnelt, M. G., & Rees, M. J. 1993, MNRAS, 263, 168
Haring, N., & Rix, H. W. 2004, ApJ, 604, 89
Hemsendorf, M., Sigurdsson, S., & Spurzem, R. 2002, ApJ, 581, 1256
Jaffe, A. H., & Backer, D. C. 2003, ApJ, 583, 616
Janssen, G. H., Stappers, B. W., Kramer, M., Purver, M., Jessner, A., & Cognard, I. 2008, in AIP Conf. Proc. 983, 40 Years of Pulsars: Millisecond Pulsars, Magnetars and More, ed. C. Bassa et al. (Melville, NY: AIP), 633
Jenet, F. A., Hobbs, G. B., Lee, K. J., & Manchester, R. N. 2005, ApJ, 625, 123
Jenet, R., et al. 2009, arXiv:0909.1058
Lauer, T. R., et al. 1995, AJ, 110, 2622
Lazio, J. 2009, in Proc. of Panoramic Radio Astronomy: 1-2 GHz Research on Galaxy Evolution, ed. G. Heald & P. Serra, http://pos.sissa.it/cgi-bin/reader/conf.cgi?confid=89, id.58
Lightman, A. P., & Shapiro, S. L. 1977, ApJ, 211, 244
Lodato, G., Nayakshin, S., King, A. R., & Pringle, J. E. 2009, MNRAS, 398, 1392
Madau, P., & Rees, M. J. 2001, ApJ, 551, 27
Magorrian, J., et al. 1998, AJ, 115, 2285
Makino, J., & Funato, Y. 2004, ApJ, 602, 93
Manchester, R. N. 2008, in AIP Conf. Proc., 983, 40 Years of Pulsars: Millisecond Pulsars, Magnetars and More, ed. C. Bassa et al. (Melville, NY: AIP), 584
Matsubayashi, T., Makino, J., & Ebisuzaki, T. 2007, ApJ, 656, 879
Merritt, D., Mikkola, S., & Szell, A. 2007, ApJ, 671, 53
Merritt, D., & Poon, M. Y. 2004, ApJ, 606, 788
Merritt, D., & Quinlan, G. D. 1998, ApJ, 498, 625
Merritt, D., & Szell, A. 2006, ApJ, 648, 890
Mikkola, S., & Valtonen, M. J. 1992, MNRAS, 259, 115
Milosavljevic, M., & Merritt, D. 2001, ApJ, 563, 34
Milosavljevic, M., & Merritt, D. 2003, ApJ, 596, 860
Perets, H. B., & Alexander, T. 2008, ApJ, 677, 146
Peters, P. C., & Mathews, J. 1963, Phys. Rev., 131, 435
Porter, E. K., & Cornish, N. J. 2008, Phys. Rev. D, 78, 4005
Porter, E. K., & Sesana, A. 2010, PhRvD, submitted (arXiv:1005.5296)
Quinlan, G. D. 1996, New Astron., 1, 35
Rest, A., van den Bosch, F. C., Jaffe, W., Tran, H., Tsvetanov, Z., Ford, H. C., Davies, J., & Schafer, J. 2001, AJ, 121, 2431
Rhook, K. J., & Wyithe, J. S. B. 2005, MNRAS, 361, 1145
Sesana, A., Haardt, F., & Madau, P. 2006, ApJ, 651, 392 (SHM06)

Sesana, A., Haardt, F., & Madau, P. 2008, ApJ, 686, 432 (SHM08)

Sesana, A., Haardt, F., Madau, P., & Volonteri, M. 2004, ApJ, 611, 623

Sesana, A., Haardt, F., Madau, P., & Volonteri, M. 2005, ApJ, 623, 23

Sesana, A., & Vecchio, A. 2010, Phys. Rev. D, 81, 4008

Sesana, A., Vecchio, A., & Colacino, C. N. 2008, MNRAS, 390, 192

Sesana, A., Vecchio, A., & Volonteri, M. 2009, MNRAS, 384, 2255

Sesana, A., Volonteri, M., & Haardt, F. 2007, MNRAS, 377, 1711

Tremaine, S., et al. 2002, ApJ, 574, 740

Tundo, E., Bernardi, M., Hyde, J. B., Sheth, R. K., & Pizzella, A. 2007, ApJ, 663, 53

Volonteri, M., Haardt, F., & Madau, P. 2003, ApJ, 582, 599

White, S. D. M., & Rees, M. J. 1978, MNRAS, 183, 341

Wyithe, J. S. B., & Loeb, A. 2003, ApJ, 590, 691

Yu, Q. 2002, MNRAS, 331, 935

Yunes, N., Arun, K. G., Berti, E., & Will, C. M. 2009, Phys. Rev. D, 80, 4001